Composites Science and Technology 270 (2025) 111250

Contents lists available at ScienceDirect

Composites Science and Technology

journal homepage: www.elsevier.com/locate/compscitech

Notch nonlinearities in pseudo-ductile composite laminates: A novel LE/HE sublaminate design

A. Subramani [a], P. Maimí [a,*], J. Cugnoni [b], R. Amacher [c], J. Costa [a]

[a] AMADE, Escola Politècnica Superior, Universitat de Girona, Girona, 17071, Spain
[b] La Haute Ecole d'Ingénierie et de Gestion du Canton de Vaud, Route de Cheseaux 1, 1400 Yverdon-les-Bains, Switzerland
[c] Laboratory for Processing of Advanced Composites (LPAC), Institute of Materials (IMX), École Polytechnique Fédérale de Lausanne (EPFL), Station 12, 1015, Lausanne, Switzerland

ARTICLE INFO

Keywords:
Pseudo-ductility
Open-hole strength
Image processing

ABSTRACT

Attempts to achieve pseudo-ductility in quasi-isotropic (QI) thin-ply laminates have traditionally relied on stacking [LE/HE/LE] sublaminates, with LE representing low-elongation and HE high-elongation. However, the increase in effective ply thickness led to reduced unnotched strength. Alternatively, in this study, we define a new sublaminate configuration ([LE/HE]) to minimise the increase in ply-block thickness and compare experimentally such hybrid QI thin-ply laminate with a conventional thin-ply QI ($\Pi/4$) laminate. The hybrid specimens demonstrated consistent but modest pseudo-ductile properties (ultimate-to-pseudo-yield strength ratio, σ_f/σ_y=1.1; pseudo-ductile strain, ϵ_d=0.3%). Using Digital Image Correlation (DIC) and advanced dark-field X-ray imaging, we detected earlier and more pronounced deviations from linear strain fields in hybrids compared to the reference laminates. The hybrid laminates showed an 11.7% reduction in unnotched strength but a 4% increase in notched strength in Open-Hole Tension (OHT) specimens. Thus, the proposed hybridisation introduces new damage mechanisms facilitating stress redistribution, thereby recovering more nominal strength with a reduced impact on the unnotched strength. Our findings suggest viable approaches to integrate pseudo-ductility into thin-ply laminates whilst preserving the inherent advantages of ply thinness.

1. Introduction

Thin-ply composites (t_{ply} = 20–100 μm) exhibit less dispersion in mechanical properties than conventional composites (t_{ply} = 100–200 μm) due to their ability to delay/suppress sub-critical damage mechanisms (*e.g.,* matrix cracking, longitudinal/off-axis splits). However, this reduced sub-critical damage limits the stress redistribution around notches, amplifying notch sensitivity [1,2]. Consequently, strategies to mitigate the inherent brittleness of thin-ply laminates are of significant interest.

Hybridisation, combining plies of different failure strains, is a promising approach to counteract brittleness in thin-ply laminates [3,4]. Orientation-blocked ply-by-ply hybridisation of low elongation (LE) and high elongation (HE) plies as [HE/LE/HE] sublaminate is the most prevalent design [3–5]. It aims to induce LE layer fragmentation and delamination upon loading. Subsequent loading saturates this damage, transferring the load to neighbouring HE layers and resulting in pseudo-ductile behaviour (Fig. 1). This pseudo-ductile behaviour extends to quasi-isotropic (QISO) laminates (orienting the HE/LE/HE sublaminates in the desired QISO configuration), albeit with a negligible plateau due to varied fragmentation onset [6,7] (Fig. 1).

Indeed, Czél et al. [6], Fotouhi et al. [8], and Tavares et al. [5] report reduced notch sensitivity in hybrid laminates. However, Tavares et al. [5] highlight the limitations of using small, single-notch specimens for this assessment, observing that the notch sensitivity reduction decreases with increasing specimen size. This may be attributed to the size-effect – notched strength decreases with scaled-up specimens, even with constant geometric ratios and material properties – of quasi-brittle materials [9,10]. Thus, the notch sensitivity characterisation require multiple size test campaign, this approach would be cumbersome. Therefore, an alternative approach is needed to gauge notch sensitivity reduction in pseudo-ductile laminates effectively.

The observed reduction in notch sensitivity may be attributed to pseudo-ductility, but also to the increase in the effective ply thickness involved in orientation-blocked designs, and their corresponding damage mechanisms. Increased ply thickness has been shown to decrease the stress concentration factor (K_t) [11,12]. Therefore, this manuscript aims to shed light in differentiating pseudo-ductile damage mechanisms from those of conventional laminates.

* Corresponding author.
E-mail address: pere.maimi@udg.edu (P. Maimí).

https://doi.org/10.1016/j.compscitech.2025.111250
Received 16 December 2024; Received in revised form 19 May 2025; Accepted 21 May 2025
Available online 9 June 2025

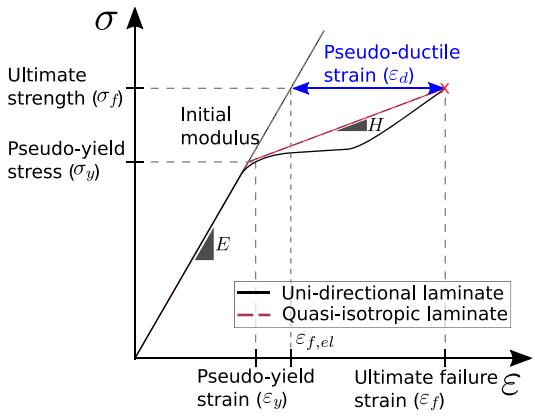

Fig. 1. Representative uni-axial tensile response of unidirectional and quasi-isotropic pseudo-ductile composite laminates. E and H represent the elastic and "Hardening" modulus. $\varepsilon_{f,el}$ represent the pseudo-elastic strain at the unnotched strength, σ_f.

Table 1
Tested quasi-isotropic laminates and their stacking sequences. LE and HE refer to low-elongation (HR40) and high elongation (T800) materials, respectively. The orientations in bold represent a typical sublaminate. Note that the hybrid laminates mid-ply sublaminate block is not repeated.

Material	Stacking sequence
T800	$[45/90/-45/0]_{4S}$
T800/HR40	$[45_{HE}/45_{LE}/90_{HE}/90_{LE}/-45_{HE}/-45_{LE}/\mathbf{\bar{0}_{HE}}/\mathbf{\bar{0}_{LE}}]_{4S}$

Considering that orientation-blocked pseudo-ductile laminates may also exhibit reduced unnotched strength due to increased ply thickness [13,14], we search for a trade-off between pseudo-ductility and unnotched strength and demonstrate it by testing a reference laminate (HE plies of the same laminate stacking sequence), something that was not done in [6] or [8]. Though a sublaminate-based all-carbon laminate tested by [15] demonstrated impressive pseudo-ductility and almost no notch-sensitivity, it suffered from a load drop at the onset of pseudo-yield, and its ultimate strength was severely reduced.

We evaluated the hybridisation effects by means of unnotched (σ_f) and notched strengths (σ_N) of both reference and hybrid laminates and studied their strain field non-linearities with Digital Image Correlation (DIC). Our approach distinguished pseudo-ductile strains from those caused by damage. Advanced X-ray imaging analyses further corroborated the experimental full-field DIC data. The methodology section (Section 2) details materials, laminate design, testing, DIC and X-ray damage characterisation. The results section (Section 3) presents load–displacement or stress–strain curves, post-mortem OHT images, processed DIC images, and X-ray findings.

In summary, we demonstrate how pseudo-ductility can be achieved using an LE/HE sub-laminate design. The hybrid laminates are compared to a reference laminate, revealing a slight reduction in unnotched strength but comparable OHT strength. Additionally, we showcase the use of DIC to characterise strain non-linearities, pseudo-ductile strains, and damage.

2. Materials and methods

2.1. Laminate design

This study utilised T800-TP175 and HR40-TP175 thin ply carbon pre-pregs, both produced by NTPT (Renens, Switzerland) using spread tow technology. T800 is an intermediate modulus carbon fibre and its UD composite has a ply thickness of 67 μm and reaches an elastic modulus, E, of 294 GPa and a failure strain, ε_f, of 1.9%. Conversely, HR40 is a high-modulus carbon fibre and its UD composite has a ply thickness of 20 μm and reaches an elastic modulus of 375 GPa and a failure strain of 1.2%. Thus, HR40-TP175 qualifies as LE material, while T800-TP175 is a HE material. Both the prepregs are targeted to a volume fraction (V_f) of 55 ± 2% by the supplier.

Our primary focus in designing the hybrid laminate was to achieve pseudo-ductility while maintaining the unnotched strength near to that of the reference LE laminate and minimising inter-sublaminate delamination at the HE/LE interfaces before failure. Such constraints inevitably limit the achievable pseudo-ductility, as it depends on inducing dispersed delamination to increase the ultimate failure strain. Moreover, the pseudo-ductile laminate's damage onset, σ_y, must be sufficiently higher than that of an equivalent thick-ply laminate to retain the benefits of thin-ply laminates. Following the principles of Jalalvand's shear-lag model [16], we sought to satisfy these requirements simultaneously and was determined that grouping one 20 μm ply of HR40 with one 68 μm ply of T800 – a [HE/LE] sublaminate – satisfies all of the above. For detailed information, refer to [17]. Through automated tape laying, NTPT manufactured hybrid pre-preg rolls in 0/0 or 0/90 orientations of [HE/LE], which we used to form the hybrid QISO laminates.

Following manufacturer recommendations, we autoclave-cured (180 °C for 6 h at 6 bar) two quasi-isotropic ($\Pi/4$) laminates (see Table 1): a 2.19 mm thick reference laminate using T800-TP175 in a $[45/90/-45/0]_{4S}$ stacking sequence, and a 2.67 mm thick hybrid laminate with the same stacking sequence but incorporating [HE/LE] sublaminate plies for pseudo-ductility. Both pre-pregs used the same toughened multi-functional high-strength resin system, TP175, developed by NTPT for compatibility. The V_f of the laminate was calculated using the fibre areal weight data (provided by the supplier for each prepreg), resin density and the cured laminate thickness. The mean values of the calculated V_f was 55.4 ± 2% for both the laminates.

2.2. Unnotched and open-hole tests

Unnotched tensile (UNT) and open-hole tensile (OHT) tests were performed following ASTM D3039/D3039M-17 [18]. The specimen size was 240 mm by 24 mm (gauge length and width, respectively). UNT samples were equipped with tapered glass-epoxy end tabs (Fig. 2a). OHT tests followed ASTM D5766/D5766M-11(2018) [19]. The OHT samples maintained the UNT specimens' gauge length but differed in width, 36 mm with a 6 mm hole diameter (conventional diameter-to-width ratio of 1/6), see Fig. 2a. Tests were carried out on an MTS 809 hydraulic testing machine with a 100 kN load cell at a constant loading rate of 2 mm min^{-1}. UNT samples were monitored with strain gauges, while OHT specimens relied on the testing machine's LVDT for the displacement (u). The net-section failure stress of OHT specimens' is,

$$\sigma_N = \frac{P_u}{A_{net}} = \frac{P_u}{(W-2R)t} \tag{1}$$

where P_u is the failure load, $A_{net} = (W-2R)t$ is the net-section area, and W and t are the specimen's width and thickness, respectively.

2.3. Digital Image Correlation (DIC)

A fine speckle pattern, applied with spray paint on one side of the OHT specimens, enabled DIC visualisation through VIC-2D software [20]. The specimens were observed with a 1.3 Mpx camera (Allied Vision Guppy F146) in a close-up view centred on the central hole for a typical pixel size of 0.0338 mm. The software effectively reconstructed full-field displacement/strain across a 36 × 36 mm window surrounding the hole. The processing parameters were a subset size of 17 pixels, a step size of 5 pixels, and a strain filter size of 5 pixels. This full-field strain data served as a virtual extensometer (correcting machine compliance in OHT samples without strain gauges) and determined the regions of strain nonlinearity.

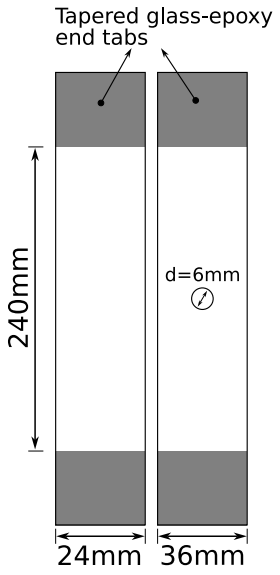

Fig. 2. Representative sample dimensions for both unnotched and open-hole tensile tests. Note: The gauge lengths for unnotched and notched specimens are identical.

2.3.1. Compliance correction of OHT tests

We used DIC as a virtual extensometer to correct the load–displacement curve of OHT tests for the machine compliance (C_m), P-u_r. DIC images and load cell data were carefully synchronised. Then, the average strain, $\bar{\varepsilon}_{yy}$ [21], in the region of interest, is,

$$\bar{\varepsilon}_{yy} = \frac{\Delta l}{l_{\mathrm{DIC}}} \tag{2}$$

where l_{DIC} is the distance from the topmost to the bottommost pixel in the region of interest, and Δl signifies the relative increase in specimen length. Δl is calculated as the absolute difference in displacements between u_{top} and u_{bot}. We consider u_{top} and u_{bot} to be the average displacements (along the specimen width) along pixel rows at the top and bottom. These average displacements are sufficiently distant from the hole to not be influenced by the regions of stress concentration (the hole). Assuming $\bar{\varepsilon}_{yy}$ to be equivalent to the average specimen strain, ε_{yy}, the actual specimen compliance, C, can then be determined. Thus, the displacement corrected for the machine compliance, u, is,

$$u = u_r - P \times C_m \tag{3}$$

where $C_m = C_r - C$, C_r is the compliance measured by the load-cell.

2.3.2. Strain deviation from linearity

When the applied load is small, all material points of the specimen remain within the elastic regime. The stress concentration factor (K_t) indicates the stress increase at the hole edge. Then, for the material to maintain its elastic behaviour, any applied stress must be less than σ_y/K_t, where σ_y represents the material's elastic limit (refer to Fig. 1). In terms of the external load:

$$P_{el} < \frac{\sigma_y A_{net}}{K_t} \tag{4}$$

and then, for linear materials, the stress and strain fields remain proportional. By proportionally scaling these strain fields to any load level, the deviations between the scaled strains and those observed by DIC reveal the regions of strain nonlinearities. Remarkably, this identification can be done without the comprehensive knowledge of the materials' constitutive behaviour. Such nonlinearities can arise from failure process zones, longitudinal or off-axis splits, delamination in standard composite laminates, and fragmentation or dispersed delamination in hybrid materials.

The principal DIC strain in the y-direction for a load P_{el} is the elastic strain, $\varepsilon_{yy,P_{el}}$; and the strain non-linearity for a load P_i above P_{el}, ε_{nl,P_i}, reads,

$$\varepsilon_{nl,P_i} = \varepsilon_{yy,P_i} - \frac{P_i}{P_{el}} \times \varepsilon_{yy,P_{el}} \tag{5}$$

We represent all the full-field data using a perceptually uniform colour map like *viridis*, to ensure an objective, consistent, and accessible representation of the data [22].

2.3.3. Pseudo-ductile strain and damage from full-field DIC strains

Using the ultimate pseudo-ductile strain, ε_d, one can effectively gauge the additional failure strain increase brought on by hybridisation [4,6,16], as shown in Fig. 1. Essentially, ε_d is the difference between the failure strain, ε_f, and the strain observed in a corresponding pseudo-elastic material at the unnotched strength, $\varepsilon_{f,el} = \sigma_f/E$, *i.e.*,

$$\varepsilon_d = \varepsilon_f - \varepsilon_{f,el} \tag{6}$$

Eq. (6) represents the pseudo-ductile strain at failure, as in Fig. 1. The pseudo-ductile strain at a specific load level, σ_i, can also be incrementally defined as,

$$\varepsilon_{d_i} = \varepsilon_i - \sigma_i/E \tag{7}$$

where σ_i and ε_i represent the stress and strain. Further, after "yielding", we assume that the laminate behaves as an idealised pseudo-ductile material with "hardening-modulus", H, defined as,

$$H = \frac{\sigma_i - \sigma_y}{\varepsilon_i - \varepsilon_y} \tag{8}$$

where σ_y and ε_y correspond to the pseudo-yield stress and strain. By defining $h(= H/E)$ as the hardening modulus ratio and relating Eq. (8) and $\varepsilon_{i,el} = \varepsilon_y + (\sigma_i - \sigma_y)/E$, the pseudo-ductile strain in the regime $\sigma_y < \sigma_i < \sigma_f$ is,

$$\varepsilon_{d_i} = \left(\varepsilon_i - \varepsilon_y\right)(1 - h) \tag{9}$$

Note that the ε_{d_i} in Eq. (9) differ to ε_d in Eq. (6) at every load level, except when $\varepsilon_i = \varepsilon_f$, where they are identical. Calculating ε_{d_i} using Eq. (9) enables the extraction of pseudo-ductile strains from the full-field DIC strains at any load level, using ε_y and h as material properties from the UNT. Although this method aligns with the conventional approach to computing the scalar ε_d (Eq. (6), Fig. 1), factors such as cohesive regions, surface delamination, and longitudinal/off-axis splits can influence the full-field strains, and hence the resulting pseudo-ductile strain. Consequently, the pseudo-ductile strain field, ε_{d_i}, can only be considered as a qualitative indicator of the inelastic strain.

In a UNT, following the "yielding" (see Fig. 1), pseudo-ductility manifests through fibre or ply fragmentation and/or dispersed delamination [3,4,6,7]. Since, these damage mechanisms are irreversible, they aptly classify as pseudo-ductile damage. Thus, the pseudo-ductile damage, d_i, can be presented as, [23,24],

$$d_i = 1 - \frac{E_i}{E} = \frac{\varepsilon_{d_i}}{\varepsilon_i} \tag{10}$$

where E_i is the secant modulus. This method also facilitates the comparison of scalar damage variables (SDV) derived from FE models, as detailed in [24].

2.4. X-ray imaging

We conducted X-ray imaging on the OHT samples post-testing to reveal the internal damage mechanisms. The Talbot-Lau grating interferometer facilitated a combined deployment of three distinct X-ray methodologies: conventional (absorption), phase contrast (refraction), and dark field (scattering) [25]. The X-ray measurements were performed at LPAC/EPFL using the phase contrast X-ray radiography

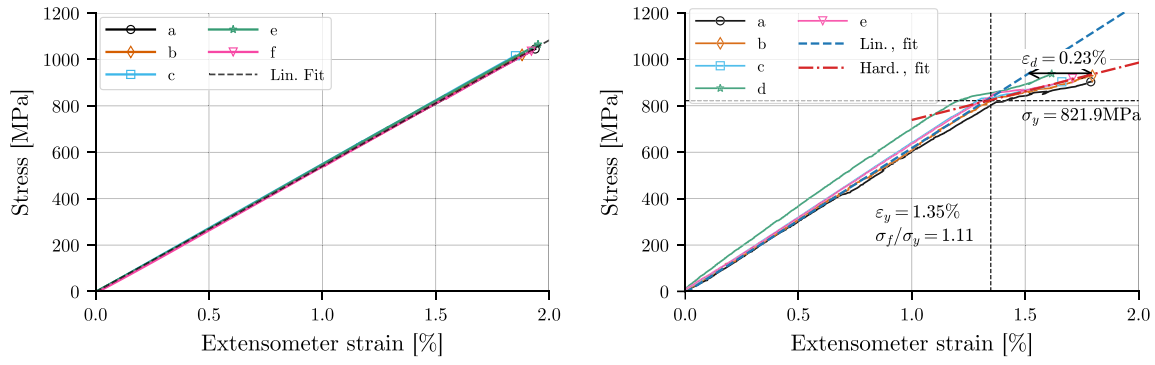

(a) T800 σ-ε (b) T800/HR40 σ-ε

Fig. 3. Unnotched tensile (UNT) response of the reference (T800) and hybrid (T800/HR40) quasi-isotropic laminates. (a) and (b) display the σ-ε values, with ε recorded by the strain-gauges. Note that the two laminates vary in thickness.

equipment which was a product of the EVITA initiative [26]; for further information, refer to [27]. We utilised dark-field imaging, or small-angle scattering X-ray imaging, known for its ability to capture high-contrast images, ideal for characterising pseudo-ductile damage mechanisms. This method is particularly adept at highlighting intricate details such as cracks or small heterogeneities.

A particular aspect of this phase contrast X-ray imaging technique is that the contrast depends on the orientation of the interfaces or cracks with respect to the grating. Thus, we subjected both a reference and a hybrid specimen to X-ray examination across three planar orientations (x-y plane): 0°, 45°, and 90°. After this, we equalised the grey-scale values of each orientation's images, assigning a dedicated colour channel. We then superimposed these images, adjusting the transparency to 50% for the 45° and 90° images. The combined image nearly encapsulates all the identifiable features. Note that, we captured these X-ray images when the samples were completely broken, post-failure.

3. Results

3.1. Unnotched strength

In Fig. 3, we present the stress–strain (σ-ε) curves for both QISO laminates from the UNT tests (load–displacement curves of these laminates can be found in the supplementary information). The scatter in the ultimate load is very low for both laminates.

The hybrid laminate exhibits nonlinearity around the peak load, whereas the reference laminates does not. To highlight the nonlinearity, Fig. 3a and b incorporate a linear line representing the average elastic modulus. Classical Laminate Theory (CLT) predicts elastic modulus values of 56 GPa for T800 laminates, 69.4 GPa for HR40 laminates, and 59.4 GPa for the hybrid (T800/HR40) laminate. Our experimental results align closely with these predictions for both the reference and hybrid laminates, showing 3% and 5% deviations, respectively.

Regarding the nonlinear behaviour of the hybrid T800/HR40 laminates (Fig. 3b), we have defined a 0.1% strain offset as the yielding point; thus, the pseudo-yield strain, ε_y, is 1.35%. While ε_y typically aligns with ε_f of the LE, here it surpasses the HR40 fibres' ε_f (1.2%) by 14%. This rise implies that the HE (T800) plies synergistically counteract the pronounced brittleness of the LE plies. Despite that, hybrid laminates reveal consistent nonlinearities post the pseudo-yield strain, indicating load redistribution. Moreover, the failure strain, ε_f = 1.75%, approaches that of T800's ε_f = 1.9%. This underscores the synergistic interaction between LE and HE materials: fragmentation in the LE layers (HR40) does not trigger an immediate laminate failure – a behaviour observed in certain pseudo-ductile laminates [8]. Thus, the ultimate ε_d, as per Eq. (6) (Fig. 1), is 0.23%, a considerably lower value in comparison to the laminates tailored for pseudo-ductility (ε_d = 1%–2% [6,8]). Indeed, we designed the hybrid laminates to achieve a high damage onset (≈800 MPa for a quasi-isotropic laminate) to balance strength and pseudo-ductility. Sample d (Fig. 3b) of the hybrid laminates is an exception due to its unusually high elastic modulus, but its pseudo-ductile features persist.

In comparing the unnotched strengths (σ_f) between the reference and hybrid laminate, hybridisation results in an 11% reduction in strength $(\sigma_f)_{\text{ref}}/(\sigma_f)_{\text{pd}}$. The LE (HR40) plies do contribute to the ultimate strength. Indeed, the expected UNT strength assuming that only the HE fibres support the load upon LE ply failure would be 808.4 MPa ($(V_f)_{HE} * (\sigma_f)_{HE}$ = 0.78*1036.4 MPa), while the experimental strengths are 13% higher (919.36/808.4 MPa). The idealised stress–strain curves from the average values of the experimental test results (Fig. 3) for both the reference and hybrid laminates are presented in the supplementary information.

3.2. Open-hole strength

Fig. 4 presents the stress–strain curves (compliance corrected according to Section 2.3.1) for the reference and hybrid laminates. A linear reference line, based on average slopes from the σ-ε curves, facilitates the assessment of the point of nonlinearity. The hybrid laminate initiates its nonlinearity earlier than the reference laminate, and redistributes the stresses. Fig. 4 also presents the onset of nonlinearity, specifically the "elastic" load level, P_{el} (= σ_f/K_t^E).

Post-mortem images (Fig. 5) consistently reveal similar failure modes, demonstrating the repeatability of thin-ply laminates. Each specimen experiences net-section failure from the stress concentration, *i.e.*, the hole. And, each laminate type exhibits a distinct failure mode: net-section failure perpendicular to loading in the reference laminate, and off-axis failure initiating from the notch in the hybrid laminate. The presence of the notch causes a reduction in notched strength (σ_f/σ_N) by 40% in the reference laminate and 30% in the hybrid, see Table 2. While hybridisation decreases the unnotched strength, σ_f, by 11%, it enhances the nominal strength retention by 10% – $(\sigma_N/\sigma_f)_{\text{pd}} - (\sigma_N/\sigma_f)_{\text{ref}}$, see Fig. 6. This is substantiated by the nearly equal notched strengths, $(\sigma_N)_{\text{ref}}/(\sigma_N)_{\text{pd}}$ of both laminates (within 4%). This heightened nominal strength retention is likely due to the additional damage mechanisms brought on by hybridisation, which will be identified in the subsequent sections using both DIC and X-ray techniques.

3.3. DIC strain fields

3.3.1. Overall strain fields at peak-loads

To establish a benchmark, Fig. 6 presents full-field y-direction principal strain values just before peak load for reference and hybrid

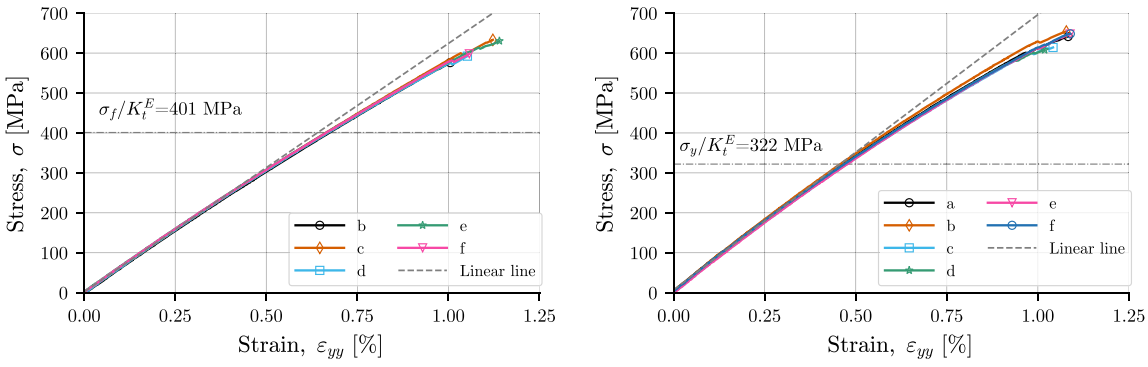

(a) T800 σ-ε (b) T800/HR40 σ-ε

Fig. 4. Open-Hole Tensile (OHT) behaviour of both the reference (T800) and hybrid (T800/HR40) quasi-isotropic laminates. (a) and (b) show the σ-ε relationship, with ε deduced by adjusting the u using specimen compliance identified via DIC. Note that the reference and hybrid laminates vary in thickness.

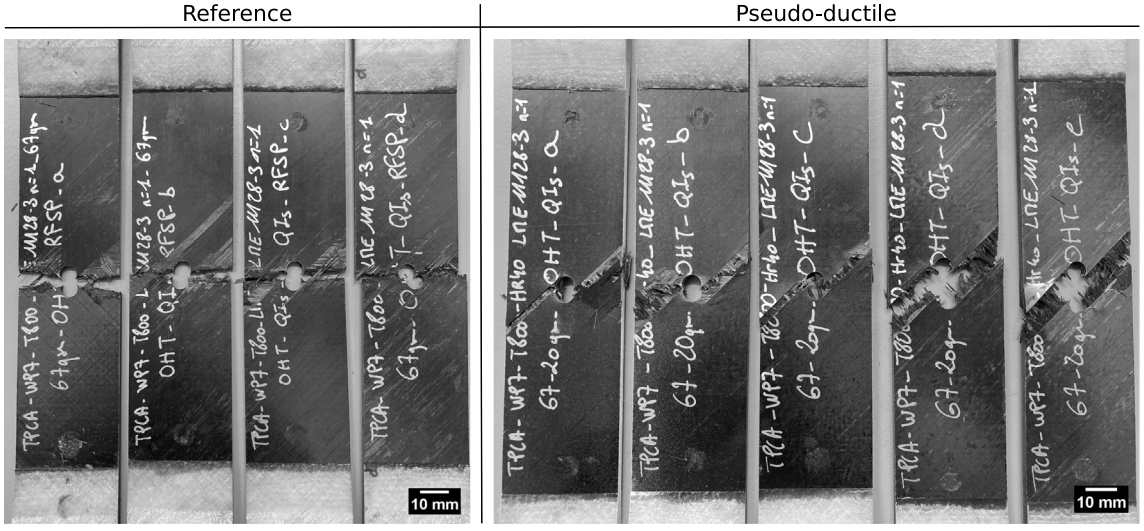

Fig. 5. Post-mortem images of the failed quasi-isotropic open-hole specimens of the reference (T800), and hybrid (T800/HR40) laminates.

Table 2
Quasi-isotropic mechanical properties of the baseline and hybrid laminates from unnotched and open-hole tensile tests.

Material property	T800 (reference)	T800/HR40 (hybrid)
Ply thickness, t_{ply} [µm]	67	67/20
Elastic modulus (fibre)[a], E_{11} [GPa]	294	294/375
Tensile failure strain (fibre)[a], ε_f [%]	1.9	1.9/1.2
Volume fraction (ply)[a], V_f [%]	55 ± 2	55 ± 2
Laminate thickness, t [mm]	2.19	2.67
Elastic modulus, E_{11} [GPa]	54.25 ± 0.52	62.37 ± 1.9
Long. tensile strength, σ_f [MPa]	1036.4 ± 19.9	914.36 ± 12.7
Long. failure strain, ε_f [%]	1.9 ± 0.04	1.75 ± 0.06
Pseudo-yield strength, σ_y [MPa]	–	831.9 ± 14
Pseudo-yield strain, ε_y [%]	–	1.35 ± 0.03
Pseudo-ductile strain, ε_d [%]	–	0.23 ± 0.03
Initiation toughness[b], $\mathcal{G}_{I0}$ [kJ m^{-2}]	61	64
Steady-state toughness[b], $\mathcal{G}_{Ic}$ [kJ m^{-2}]	106.91 ± 5.55	121.47 ± 12.43
Open-hole tensile strength, σ_N [MPa]	617.92 ± 34.91	641.96 ± 24.02

[a] From Cugnoni et al. [14].
[b] From Cugnoni et al. [17] for the same laminates.

laminates. Normalised full-field strains use average ε_f from the unnotched tensile tests (Section 3.1). Regions exceeding ε_f, *i.e.*, $\varepsilon_{ii}/\varepsilon_f > 1$, are shaded grey, highlighting highly damaged or cohesive zones. DIC strain maps of quasi-isotropic laminates reveal that surface strain patterns primarily reflect the surface ply orientation, while subsurface layers shape the nuances of developed damage in the later loading stages [28]. With similar surface plies (45°) in both QISO laminates (see Table 1), differences in strain fields likely arise from the laminates' intrinsic characteristics.

DIC strain fields, captured just before peak loads, hardly reveal sub-critical damage mechanisms induced by hybridisation. This is due to the cohesive zones (or transverse/translaminar cracks) dominating the failure plane around peak load, making the distinction between cohesive damage and other mechanisms difficult in small specimens – a consequence of the size effect [9,29].

Normalised full-field strains remain consistent between samples in both reference and hybrid laminates (Fig. 6). The hybrid laminate exhibits larger damage patterns (grey areas), with off-axis splits, which are absent in the reference laminate as denoted by the grey semi-circular shape. This variation in damage mechanisms correlates with the change in failure modes depicted in Fig. 5.

3.3.2. Strain deviation from linearity

To identify nonlinear strains, we first determine the elastic load level (P_{el}) as outlined in Section 2.3.3. Assuming linear-elastic material, the elastic stress concentration factor (K_t^E) for the test configuration (2R/W = 1/6) is 2.584 [24,30]. From this, the elastic loads are 26.35 kN and 25.78 kN for the reference and hybrid OHT specimens, respectively — derived from $[\sigma_i(W-2R)t]/K_t^E$, where, σ_i is σ_f and σ_y for the respective laminates. These elastic loads represent 65% and 50%,

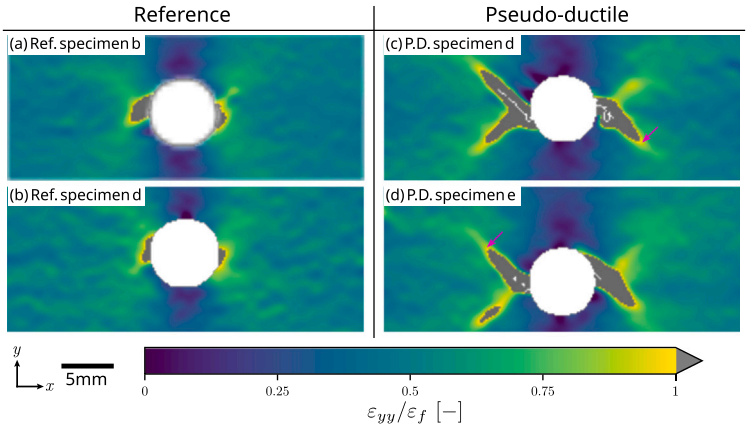

Fig. 6. Normalised full-field principal strain ($\varepsilon_{yy}/\varepsilon_f$) captured by DIC just before the peak load (P_u) for both reference and hybrid laminates. Both OHT specimens, reference and hybrid, are anticipated to fail shortly after. Principal strains are normalised using their corresponding average unnotched strains (ε_f).

respectively, of the average peak loads, exhibiting minimal nonlinearity in the σ-ε curve (Fig. 4).

From P_{el}, the incremental strain deviation to linearity ($\varepsilon_i - \varepsilon_{i,el}$) is displayed in Fig. 7 for both laminates. Areas exceeding the average pseudo-ductile strain threshold ($\varepsilon_d = 0.4\%$) are highlighted in grey in Fig. 7*A* and *B*, likely denoting zones dominated by cohesive mechanisms (crack formation, bridging, or delamination). Observing the initial frame *a* in Fig. 7*A* and *B* shows no concentrated nonlinear strains, validating the elastic load estimation method. From frame *c* ($0.75P_u$), nonlinear strain appears in both laminates. However, the reference laminate shows limited strain redistribution and cohesive zone development, even at 96% P_u (frame *e*, Fig. 7*A*), aligning with the characteristic behaviour of thin-ply laminates [13]. On the other hand, the hybrid laminate, Fig. 7*B*, exhibits marked strain nonlinearities from 75% P_u, with progressive expansion of nonlinear strain regions. However, a sharp contrast between consecutive frames (*e* and *f*) indicates that, while hybridisation enhances strain redistribution, cohesive damage mechanisms dominate around peak load.

3.3.3. Pseudo-ductile strain and damage from strain fields from DIC

We present the incremental pseudo-ductile strains and damage, derived from full-field strains in Fig. 8. Comparing the strain deviation from linearity (Eq. (5) in Fig. 7*B*) with pseudo-ductile strains in the hybrid laminate (Eq. (9) in Fig. 8*A*), reveals similar, albeit slightly narrower, pseudo-ductile regions. This aligns with expectations as Eq. (5) encompasses all nonlinearities, whereas pseudo-ductile strains before ε_y are zero in Eq. (9). Purple arrows (1) highlight specific examples in both Figs. 7*B* and 8*A*.

Pseudo-ductile strains and damage in Fig. 8*A* and *B* align closely, as expected, since one delineates the pseudo-ductile strain while the other quantifies it in terms of damage. Analysing Fig. 8*A* (frames *a* and *b*), lower ε_d or damage (coloured regions) typically precede greyed regions, suggesting that reduced stiffness areas caused by pseudo-ductile damage influence crack propagation. Despite more damage mechanisms in the hybrid laminate, the marked difference between frames at 95% P_u and P_u (frames *c* and *d* of Fig. 8*A*) emphasises the rapid growth of the cohesive region's role around P_u. Orange arrows (2) indicate failed cohesive zones (open cracks).

3.4. Damage mechanisms revealed by X-rays

Appendix A presents the different x-ray techniques (absorption, refraction and scattering) of OHT specimens from an experimental campaign on a QISO laminate ($[45/90/-45/0]_{4S}$) with a 268 μm ply-thickness [14]. It reveals that scattering (dark-field) images excel in delineating most mechanisms, corroborating prior findings [26]. Thus, only scattering images from the current OHT samples are presented, supplemented with microscopic observations in Fig. 9. Composite images (coloured and stacked grey-scale images from different X-ray orientations) provide a complete view of the observed features (see Fig. 9).

Fig. 9 reveals a predominantly flat failure plane for the reference laminate, lacking damage mechanisms like longitudinal and off-axis splits (conventional OHT laminates Fig. A.11), underscoring the brittle character of thin-ply laminates. This is corroborated by microscopy, which reveals a near-intact failure plane with minimal delamination and pull-out. Hybridisation, however, introduces sub-critical damage, evidenced by the increased damage features on the failure plane (white arrows) (Fig. 9d). Indeed, X-ray imaging reveals a significantly prominent cohesive fracture process zone (pull-out and multiple transverse splits), indicating enhanced translaminar fracture toughness compared to the reference laminate.

While DIC full-field strain data (Figs. 6 to 8) suggests secondary perpendicular off-axis splits, they are not visible in X-ray images (red arrow in Fig. 9d). This may be due to the secondary split closing when the primary split reaches a critical crack-opening state. However, this advanced x-ray analysis lacks the resolution to reveal fibre/ply fragmentation associated with pseudo-ductility.

4. Discussion

Thin-ply laminates are inherently brittle because they limit the development of subcritical damage mechanisms. Incorporating HR40 layers (high stiffness and low ultimate strain), increases the sublaminate (hybrid ply) thickness by 30%, raising elastic stiffness by 18% but reducing ultimate strength and ultimate strain by 12% and 7.9%, respectively. Nonetheless, the resulting 87 μm-thick hybrid laminate (can still be considered thin [14]), delays the matrix cracking until after HR40 fibre failure, yielding a limited pseudo-ductility. Despite this modest pseudo-ductility, the open-hole strength is 15% less sensitive to the notch, and fracture toughness increases by 14%. Consequently, hybridisation activates additional pseudo-ductile damage mechanisms, altering both crack nucleation and propagation.

Furthermore, comparing the σ_f alone of the current T800 laminate (σ_f = 1036.4 MPa) with various ply thicknesses of the same material system in [14] shows that the T800/HR40 hybrid (σ_f = 914.4 MPa) outperforms thick (268 μm, σ_f = 462 MPa) and intermediate (132 μm, σ_f = 876 MPa) laminates by +98% and +4.4%, respectively. Notably, the hybrid laminate's pseudo-yield strength exceed the thick laminate's ultimate strength and the damage onset in thick and intermediate laminates. Despite an 11.7% reduction in the UNT strength compared to the thin-ply T800 laminate, the hybrid still outperforms these traditional composites, see Fig. 10. The above mentioned values are tabulated in the supplementary information.

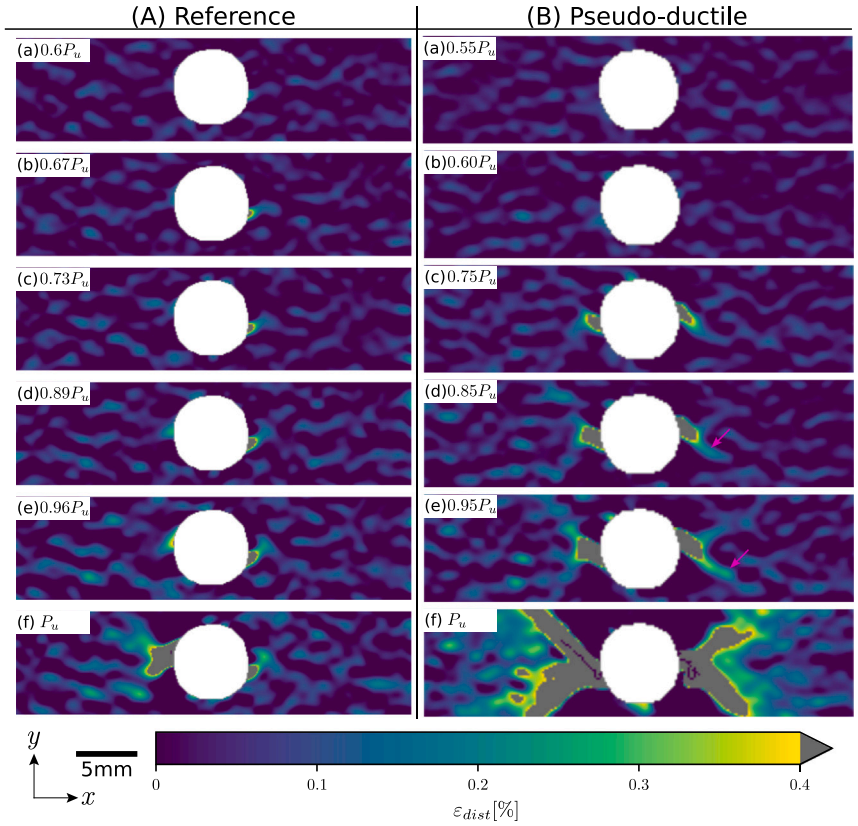

Fig. 7. Strain nonlinearities, represented as the difference between the DIC-measured principal strains and the elastically scaled strains per Eq. (5): (A) for the reference (specimen b), and (B) for the hybrid laminate (specimen d).

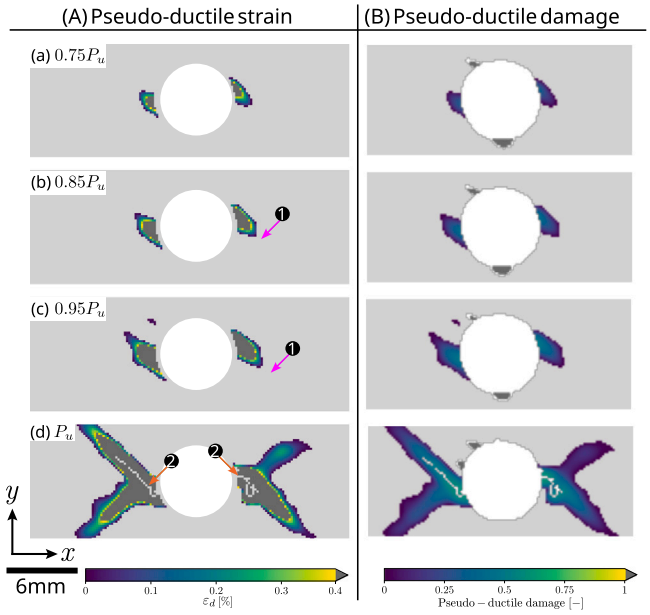

Fig. 8. Illustration of (A) Pseudo-ductile strain as per Eq. (9), and (B) pseudo-ductile damage as per Eq. (10) for the hybrid laminate (specimen *d*) derived from DIC principal strain-fields.

Despite nearly identical laminate stacking sequences, the failure mode of the reference and pseudo-ductile OHT specimens differ. The reference laminate exhibits perpendicular net-section failure, contrasting with the off-axis net-section failure in the pseudo-ductile laminate (Fig. 5). This shift may primarily be attributed to two factors. Firstly, the thicker ply blocks (or sublaminates) in the pseudo-ductile laminate (87 μm vs. 67 μm in the reference laminate) likely result in reduced failure strength due to the *in-situ* effect and may promote delamination, facilitating transverse splits in off-axis plies. Secondly, failure initiation in the pseudo-ductile laminate is marked by an off-axis crack originating at the hole and a concurrent stiffness change ahead of the crack (arrows in Fig. 6). The interaction between off-axis crack propagation and the advancing pseudo-ductile region ahead of the 45° cracks introduce mode mixity into the fracture process. Given the 45° failure plane, this crack orientation is hypothesised to exhibit lower mixed-mode toughness than the 90° failure plane. These factors collectively lead to the observed change in damage mode in the pseudo-ductile laminate.

Determining whether hybridisation confers clear benefits remains challenging. Here, we examine it through the failure of large specimens, where nominal strength is defined as the point where σ_f is reached at the specimen's maximum stressed location. Based on the numerical results of [24], the nominal strength is defined as σ_f/K_t, where the K_t values are 2.584 and 2.363 for the reference and the hybrid OH specimens at the current pseudo-ductility levels. Relative to the corresponding UNT strengths, large specimen strengths are 401 ($(\sigma_f/K_t)_{\text{ref}}$ = 1036.4/2.584) and 387 MPa ($(\sigma_f/K_t)_{\text{pd}}$ = 914.36/2.363), respectively. Nearly equal large specimen strengths of the hybrid and reference laminates indicate similar notch sensitivity, thus minimal benefits from pseudo-ductility for the hybrid laminates. However, it can also be argued that the reduction in UNT strength (−11.3%), an unavoidable consequence of achieving pseudo-ductility, is counterbalanced by the decrease in K_t (−8.5%), see Fig. 10.

Regarding additional damage mechanisms to enhance damage tolerance through pseudo-ductility, Fig. 5 shows different fracture mechanisms in reference and pseudo-ductile specimens. Reference specimens exhibit limited fibre pull-out length, indicating brittle failure, consistent with the small cohesive process zone observed in DIC analysis (Fig. 6). In contrast, pseudo-ductile specimens show extensive off-axis splitting throughout the laminate thickness (Fig. 5), leading to a 45° fracture orientation. More significant pull-out length in pseudo-ductile specimens corroborates the more extensive cohesive fracture region observed through DIC (Fig. 6).

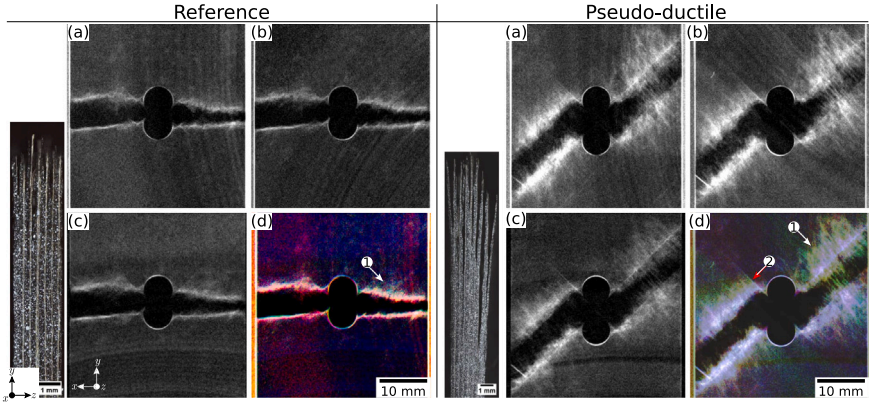

Fig. 9. Post-mortem X-ray and microscopy of a failed reference and hybrid laminates. (a–c) Raw greyscale X-ray images of each laminate with constant brightness and contrast. (d) Composite image of (a–c), with red, green, and blue channels representing each orientation.

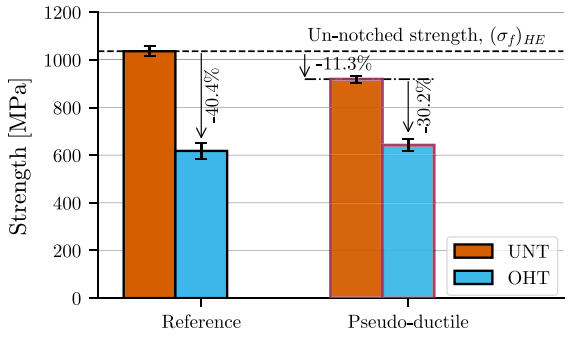

Fig. 10. Comparison of open-hole strengths (nominal) of the reference (T800) and hybrid (T800/HR40) quasi-isotropic laminates with unnotched strengths.

5. Conclusions

This study demonstrates that our novel sublaminate hybridisation method using thin plies can impart pseudo-ductility to quasi-isotropic ($\Pi/4$) composite laminates. While conventional laminates exhibited high unnotched strength (1036 MPa, approaching fibre failure strain limits), our pseudo-ductile specimens achieved consistent pseudo-ductile behaviour (pseudo-yield-to-failure stress ratio of 1.1 and pseudo-ductile strain of 0.23% at an unnotched strength of 914 MPa). This balance between unnotched strength and pseudo-ductility could be advantageous for applications where some damage tolerance is desirable while maintaining a high level of unnotched strength.

The hybrid laminate showed a limited reduction in unnotched strength (−11.3%) compared to the reference laminate. Despite this, the hybrid laminate retained 10.2% higher notched (open-hole tension) strength than the reference. Specifically, the reference laminate lost −40.4% (618 MPa) of unnotched strength, while the hybrid lost only −30.2% (642 MPa), indicating lower notch-sensitivity of the pseudo-ductile laminates.

We combined DIC and a novel X-ray technique to analyse damage mechanisms in both laminate types. DIC revealed significant differences in strain nonlinearities: reference laminates exhibited minimal nonlinearity up to 95% of ultimate load, while pseudo-ductile laminates showed early nonlinearity and broader nonlinear regions, suggesting stress redistribution due to sub-critical damage mechanisms. We further employed DIC to characterise full-field pseudo-ductile strains and incremental damage evolution. For pseudo-ductile laminates, DIC captured the progression of damage mechanisms. The X-ray technique successfully identified splits and delaminations for thicker quasi-isotropic laminates.

CRediT authorship contribution statement

A. Subramani: Writing – original draft, Writing – review & editing, Visualization, Software, Methodology, Conceptualization. **P. Maimí:** Writing – review & editing, Validation, Supervision, Resources, Funding acquisition, Conceptualization. **J. Cugnoni:** Writing – review & editing, Validation, Supervision, Resources, Investigation, Funding acquisition, Conceptualization. **R. Amacher:** Writing – review & editing, Resources, Investigation, Funding acquisition, Conceptualization. **J. Costa:** Writing – review & editing, Supervision, Resources, Funding acquisition.

Declaration of Generative AI and AI-assisted technologies in the writing process

During the preparation of this work the author(s) used ChatGPT LLM in order to improve readability and language of the written text. After using this tool/service, the author(s) reviewed and edited the content as needed and take(s) full responsibility for the content of the publication.

Declaration of competing interest

The authors declare that they have no known competing financial interests or personal relationships that could have appeared to influence the work reported in this paper.

Acknowledgements

The authors would like to acknowledge the invaluable help of Valentin Rougier, LPAC/EPFL for the phase contrast X-ray imaging. The authors acknowledge the funding and support of Ministerio de Ciencia, Innovación y Universidades, Spain for the project *En pos de materiales compuestos de fibra larga híbridos, bio-basados y sostenibles para aplicaciones estructurales, Spain* (SUBHYCO) (PID2021-126989OB-I00). Anbazhagan Subramani acknowledges the financial support of the Universitat de Girona, Spain for INV309_2019 and MOB2021. He would also like to thank the Universitat de Girona and Santander Universidades, Switzerland for the financial resources provided through *Personal Investigador en formació* (IF_UDG), 2020. Open Access funding was provided through the CRUE-CSIC, Switzerland agreement with Elsevier. The authors also acknowledge the support from North Thin Ply Technology (NTPT), Switzerland in suplying the materials and Innosuisse/CTI funding 17092.1 PFIW-IW for the experimental part of this work.

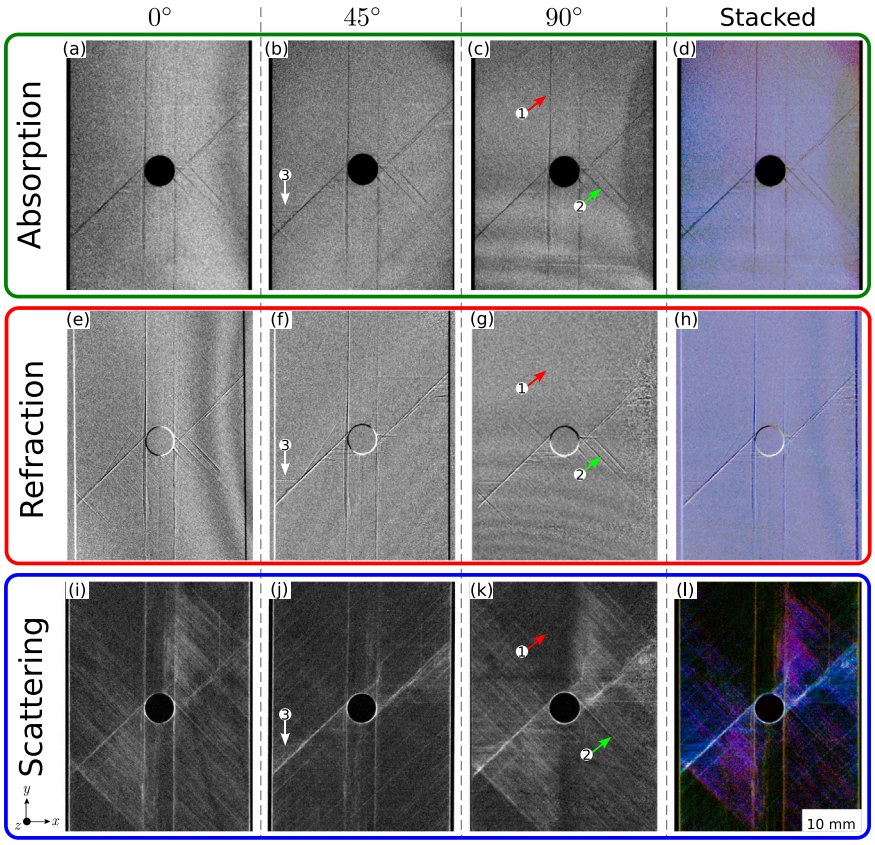

Fig. A.11. X-ray images of the failed T800-268 μm QISO laminate taken at orientations of (0°, 45°, and 90°). These angles depict the laminate's alignment in the *x*-*y* plane prior to X-ray grating. The stacked image is a composite of all three perspectives.

Appendix A. Comparison to conventional X-ray imaging

To explore the damage mechanisms unveiled by the novel X-ray imaging technique developed with EVITA [26], we X-rayed a conventional quasi-isotropic (same stacking sequence as the current study, see Table 1) OHT laminate with a ply thickness of 268 μm. This thicker sample choice aimed to uncover damage mechanisms typically recognised in composite laminates. We used the same approach as the current methodology (Section 2.4); both raw data and the composite image from various orientations can be seen in Fig. A.11.

Fig. A.11 reveals that absorption imaging is consistent across orientations, *i.e.*, showing similar damage mechanisms (orientation independent). However, with refraction and scattering displaying orientation-dependent features, only scattering reveals previously unobserved distinct damage mechanisms, offering complementary insights (compare Fig. A.11*l* to *d* and *h*). Despite its variation with orientation, refraction fails to highlight new damage mechanisms; thus, the composite of refraction and absorption is similar (Fig. A.11*d* and *h*).

Further analysing the revealed damage mechanisms, the red arrows (1) highlighting vertical splits observed in absorption imaging, for instance, are not detectable using refraction and scattering techniques when the samples are oriented in 90°. The green arrows (2) point to three minor off-axis splits emerging from the notch. While absorption images (all orientations) and refraction images (0° and 90°) detect these splits, the scattering technique identifies only one. Turning to the white arrows (3), one observes longitudinal splits from the free edges, likely emerging after the significant off-axis split is formed. This formation potentially precipitated delamination, discernible solely in the scattering technique (Fig. A.11*j* and *l*). Furthermore, the composite scattering image furnishes richer data than absorption and refraction. These observations (Fig. A.11) support the contention that increasing ply thickness accentuates these damage mechanisms, as seen when contrasting Fig. 9*d* of the reference and pseudo-ductile laminate with the laminates made of thicker plies (Fig. A.11*l*).

Appendix B. Supplementary data

Supplementary material related to this article can be found online at https://doi.org/10.1016/j.compscitech.2025.111250.

Data availability

Data will be made available on request.

References

[1] A. Arteiro, C. Furtado, G. Catalanotti, P. Linde, P. Camanho, Thin-ply polymer composite materials: A review, Compos. Part A: Appl. Sci. Manuf. 132 (2020) 105777.
[2] X. Xu, M.R. Wisnom, Y. Mahadik, S.R. Hallett, An experimental investigation into size effects in quasi-isotropic carbon/epoxy laminates with sharp and blunt notches, Compos. Sci. Technol. 100 (2014) 220–227.
[3] G. Czél, M.R. Wisnom, Demonstration of pseudo-ductility in high performance glass/epoxy composites by hybridisation with thin-ply carbon prepreg, Compos. Part A: Appl. Sci. Manuf. 52 (2013) 23–30.
[4] M.R. Wisnom, G. Czél, Y. Swolfs, M. Jalalvand, L. Gorbatikh, I. Verpoest, Hybrid effects in thin ply carbon/glass unidirectional laminates: accurate experimental determination and prediction, Compos. Part A: Appl. Sci. Manuf. 88 (2016) 131–139.
[5] R.P. Tavares, Mechanics of Deformation and Failure of Fibre Hybrid Composites (Ph.D. thesis), Universidade do Porto, Porto, Portugal, 2020.
[6] G. Czél, M. Jalalvand, M. Fotouhi, M.L. Longana, O.J. Nixon-Pearson, M.R. Wisnom, Pseudo-ductility and reduced notch sensitivity in multi-directional all-carbon/epoxy thin-ply hybrid composites, Compos. Part A: Appl. Sci. Manuf. 104 (2018) 151–164.

[7] M. Fotouhi, M. Jalalvand, M.R. Wisnom, High performance quasi-isotropic thin-ply carbon/glass hybrid composites with pseudo-ductile behaviour in all fibre orientations, Compos. Sci. Technol. 152 (2017) 101–110.
[8] M. Fotouhi, M. Jalalvand, M.R. Wisnom, Notch insensitive orientation-dispersed pseudo-ductile thin-ply carbon/glass hybrid laminates, Compos. Part A: Appl. Sci. Manuf. 110 (2018) 29–44.
[9] Z.P. Bažant, J. Planas, Fracture and Size Effect in Concrete and Other Quasibrittle Materials, Routledge, 2019.
[10] P. Maimí, E.V. González, N. Gascons, L. Ripoll, Size effect law and critical distance theories to predict the nominal strength of quasibrittle structures, Appl. Mech. Rev. 65 (2) (2013).
[11] C. Furtado, A. Arteiro, P. Linde, B. Wardle, P. Camanho, Is there a ply thickness effect on the mode I intralaminar fracture toughness of composite laminates? Theor. Appl. Fract. Mech. 107 (2020) 102473.
[12] F. Danzi, R. Tavares, J. Xavier, D. Fanteria, P. Camanho, Effects of hybridization and ply thickness on the strength and toughness of composite laminates, J. Compos. Mater. 55 (30) (2021) 4601–4616.
[13] R. Amacher, J. Cugnoni, J. Botsis, L. Sorensen, W. Smith, C. Dransfeld, Thin ply composites: Experimental characterization and modeling of size-effects, Compos. Sci. Technol. 101 (2014) 121–132.
[14] J. Cugnoni, R. Amacher, S. Kohler, J. Brunner, E. Kramer, C. Dransfeld, W. Smith, K. Scobbie, L. Sorensen, J. Botsis, Towards aerospace grade thin-ply composites: Effect of ply thickness, fibre, matrix and interlayer toughening on strength and damage tolerance, Compos. Sci. Technol. 168 (2018) 467–477.
[15] S. Sapozhnikov, S. Lomov, Y. Swolfs, V. Carvelli, Deformation and failure of pseudo-ductile quasi-isotropic all-carbon hybrid FRPS with an open hole under tension, Compos. Part B: Eng. 237 (2022) 109870.
[16] M. Jalalvand, G. Czél, M.R. Wisnom, Damage analysis of pseudo-ductile thin-ply UD hybrid composites–a new analytical method, Compos. Part A: Appl. Sci. Manuf. 69 (2015) 83–93.
[17] J. Cugnoni, G. Frossard, R. Amacher, J. Botsis, Translaminar fracture of regular and hybrid thin ply composites: experimental characterization and modelling, in: ECCM18-18th European Conference on Composite Materials, Athens, Greece, 2018.
[18] ASTM D3039/D3039M-17, Standard Test Method for Tensile Properties of Polymer Matrix Composite Materials, Technical Report, Vol. 15.03, ASTM International, West Conshohocken, PA, 2017.
[19] ASTM D5766/D5766M-11(2018), Standard Test Method for Open-Hole Tensile Strength of Polymer Matrix Composite Laminates, Technical Report, 15.03, ASTM International, West Conshohocken, PA, 2018.
[20] Correlated Solutions, VIC-2D digital image correlation, 2009, https://www.correlatedsolutions.com/vic-2d.
[21] D.E. Sommer, S.G. Kravchenko, W.B. Avery, R.B. Pipes, Mechanisms of notch insensitivity in long-fiber discontinuous, prepreg platelet compression molded composites, Compos. Part A: Appl. Sci. Manuf. 162 (2022) 107133.
[22] D. Borland, R.M.T. Li, Rainbow color map (still) considered harmful, IEEE Comput. Graph. Appl. 27 (2) (2007) 14–17.
[23] A. Subramani, P. Maimi, J. Costa, On how pseudo-ductility modifies the translaminar fracture toughness of composites and the nominal strength of centre-cracked specimens, Compos. Part A: Appl. Sci. Manuf. (2024) 108275.
[24] A. Subramani, P. Maimí, J. Guerrero, J. Costa, Nominal strength of notched pseudo-ductile specimens, Theor. Appl. Fract. Mech. (2023) 104120.
[25] T. Weitkamp, A. Diaz, C. David, F. Pfeiffer, M. Stampanoni, P. Cloetens, E. Ziegler, X-ray phase imaging with a grating interferometer, Opt. Express 13 (16) (2005) 6296–6304.
[26] M. Gresil, V. Revol, K. Kitsianos, G. Kanderakis, I. Koulalis, M.-O. Sauer, H. Trétout, A.-M. Madrigal, EVITA project: comparison between traditional non-destructive techniques and phase contrast X-ray imaging applied to aerospace carbon fibre reinforced polymer, Appl. Compos. Mater. 24 (2) (2017) 513–524.
[27] V. Revol, X-ray Phase Contrast Imaging by Grating Interferometry (Ph.D. thesis), University of Zürich, Zürich, Switzerland, 2011.
[28] F.E. Oz, M. Mehdikhani, N. Ersoy, S.V. Lomov, In-situ imaging of inter-and intra-laminar damage in open-hole tension tests of carbon fibre-reinforced composites, Compos. Struct. 244 (2020) 112302.
[29] P. Maimí, D. Trias, E. González, J. Renart, Nominal strength of quasi-brittle open hole specimens, Compos. Sci. Technol. 72 (10) (2012) 1203–1208.
[30] W.D. Pilkey, D.F. Pilkey, Z. Bi, Peterson's Stress Concentration Factors, John Wiley & Sons, 2020.